Journal of Materials Chemistry A

Accepted Manuscript

ROYAL SOCIETY OF CHEMISTRY

www.rsc.org/materialsA

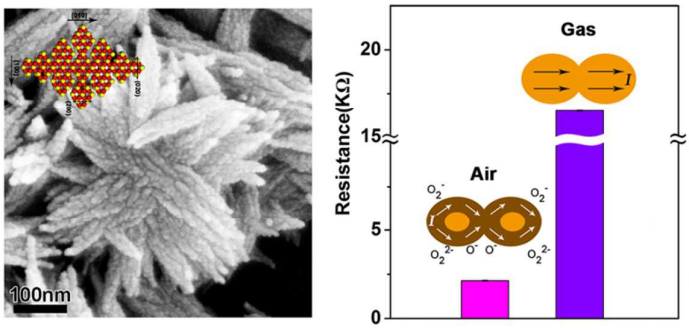

Mesocrystalline cupric oxide with pure phase and clean surface was produced by laser ablation followed by oxidization, and the gas sensor based on the mesocrystal exhibits the highest sensitivity, the fastest response, and the best selectivity ever reported towards ethanol.

Journal Name

ARTICLE

Laser synthesis of clean mesocrystal of cupric oxide for efficient gas sensing †

Received 00th January 20xx,
Accepted 00th January 20xx

DOI: 10.1039/x0xx00000x

www.rsc.org/

Zhe Li,[a] Cun-Ku Dong,[a,*] Jing Yang,[a] Shi-Zhang, Qiao,[b] Xi-Wen Du[a,*]

Mesocrystal is known as an unusual material deriving from the self-assembling of nanoparticles. Nevertheless, its advantages arising from the unique structure have not been fully exploited so far due to the obstruction of secondary phase. Herein, we employ a pulsed laser to synthesize mesocrystalline cupric oxide (CuO) with pure phase and clean surface, the gas sensor based on CuO mesocrystal exhibits the highest sensitivity, the fastest response, and the best selectivity ever reported towards ethanol. Our work elucidates the innate character of mesocrytal and clears up the doubt on its practicability.

Introduction

Mesocrystal, a concept first proposed by Cölfen in the early 2000s, is identified as a superstructure consisting of highly ordered crystalline nanoparticulates[1-3]. In contrast to common atom/ion-mediated growth[4,7], mesocrystalization generally occurs *via* the oriented alignment of nanoparticulates[6,7]. Obviously, mesocrystal materials possess large specific surface area[2,8] and high porosity[3,9], thus have been applied in lithium-ion batteries[10-13] and photodegradation[14,15]. However, their specific surface area and porosity is lower than those of the nanoparticles or aggregates, hence mesocrystals did not show obvious advantages over other materials[10-15].

Apart from the above virtues, mesocrystal materials own excellent electrical conductivity and abundant adsorption sites because of their unique architecture, which are exactly expected for gas detection[16-19]. Nevertheless, few works reported the gas sensors based on mesocrytal materials so far [20,21]. For instance, mesocrystal Cu_2O nanowires and mesocrystal α-Fe_2O_3 plates have been adopted to monitor NO_2 gas and acetone, respectively[20,21]. Nevertheless, their gas sensing performance is not as high as expected[22,23], which may arise from the existence of a continuous matrix (o-anisidine, 1-n-butyl-3-methylimidazolium chloride, etc.) for directing the ordered growth[24,25]. The matrix impedes the access of gas molecules to mesocrystals and reduces the electrical conduction, thus deteriorates the performance of gas sensors[1-3]. Hitherto, the only two template-free mesocrystal materials are Ag plates obtained by electro-deposition and ZnO microspheres by hydrothermal synthesis[26,27].

Pulsed laser ablation in liquid (PLAL) is known as a green, simple and rapid technique for the synthesis of materials. The pulsed laser can create an extremely non-equilibrium environment to produce metastable phases with clean surface and dangling bonds[28-30]. Herein, we employed PLAL method to synthesize template-free mesocrystals, where colloidal Cu_2O nanoparticles with high stability were first generated by laser ablation, and then their surface charge was partially eliminated by oxidization, leading to the self-assembly of nanoparticles and the formation of highly ordered mesocrystal CuO (M-CuO) with clean surface. We then adopted M-CuO to detect ethanol, a common target gas for CuO sensors[31-33], and M-CuO exhibits the highest sensitivity, the highest selectivity and the shortest recovery time reported so far. Density functional theory (DFT) analysis indicates that mesocrystal is more active than single crystal and polycrystal for adsorbing oxygen molecules, causing thicker depletion layers and extraordinary performance. Our results demonstrate the great potential of mesocrystal materials on the next generation of gas sensors.

Experimental section

Synthesis of M-CuO and CuO agglomerate. A top-down PLAL approach was utilized to prepare M-CuO in this study. The PLAL setup was shown in Scheme S1. Prior to PLAL, the copper target (5 mm in thickness, 20 mm in diameter) was chemically polished by using diluted hydrochloric acid (10 vol.%) for 10 min to remove oxide layer and washed by deionized water. Then the copper target was immersed in deionized water with its upper surface ~10 mm lower than the water level, and ablated for 15 min using a nanosecond pulsed Nd:YAG laser (Dawa-350, Beamtech) at pulse width 7 ns, wavelength 1064 nm, frequency 10 Hz and energy 310 mJ. The obtained Cu_2O nanoparticles were oxidized in air to produce M-CuO.

[a] *Key Laboratory of Advanced Ceramics and Machining Technology, Ministry of Education (Tianjin University), Institute of New-Energy Materials, School of Materials Science and Engineering, Tianjin University, Tianjin 300072, China*
E-mail: xwdu@tju.edu.cn; ckdong@tju.edu.cn
[b] *School of Chemical Engineering, The University of Adelaide, SA 5005, Australia*
†Electronic Supplementary Information (ESI) available: Detailed synthetic procedures, characterization methods, calculation and additional experimental results. See DOI: 10.1039/x0xx00000x

Alternatively, 5 g NaCl (0.17 M) was added into 50 ml Cu_2O colloid to arouse a rapid aggregation, then Cu_2O precipitate was oxidized in air, washed with water for several times, and dried in oven for the production of CuO agglomerate.

Synthesis of single-crystal (S-CuO) and polycrystalline (P-CuO). For the synthesis of S-CuO, 0.998 g of $Cu(Ac)_2$ was dissolved in 20 ml of deionized water, and pH value was adjusted to 11-12 by adding 0.3 mol/L NaOH[34]. The solution was magnetically stirred until a blue-white flocculent was observed. The as-prepared precipitate was then rinsed by deionized water several times, collected by centrifugation, and dried at 80 °C for 1 h to obtain S-CuO powder. For the synthesis of P-CuO, 1 g of $Cu(NO_3)_2$ was dissolved in 100 ml of deionized water, followed by the addition of 30 ml of $NH_3 \bullet H_2O$ solution (0.15 mol L^{-1}) under constant magnetic stirring[35]. NaOH solution (1 mol L^{-1}) was added dropwise with vigorous magnetic stirring to adjust the pH value to 9-10. A blue-white flocculent of $Cu(OH)_2$ was then produced. The precipitate was rinsed with deionized water, collected by centrifugation and dried in oven at 100 °C for 1 h to get P-CuO.

Characterization. The morphology of CuO samples was observed using a Hitachi S-4800 scanning electron microscope (SEM) under an acceleration voltage of 5 KV and FEI Technai G^2 F20 transmission electron microscope (TEM) equipped with a field-emission gun, and the composition was measured by an Oxford INCA energy dispersive spectrometer (EDS) attached to the TEM. The phase structure was investigated with a Bruker D8 advance X-ray diffractometer (XRD), the radiation source is CuKα light through a Ni filter. X-ray photoelectron spectroscopy (XPS) analysis was performed using a PHI Quantum 2000 scanning ESCA Microprobe spectrometer. The gas-sensing property was measured in an intelligent gas sensing analysis system (CGS-1TP, Beijing Elite Tech Co., Ltd, China). The analysis system offered an external temperature control (from room temperature to 500 °C) with a precision of 1 °C, the chamber volume was 18 L, and heating voltage changed from 0 to 25 V under different working temperature. The electrical resistance was measured by bleeder circuit and could be read directly from the computer interface. The zeta potential analysis was conducted at 25 °C using Malvern Zetasizer Nano-ZS90 (UK). The special surface area was measured at 77 K with a Quantachrome ASiQwin automated gas sorption analyzer (USA).

Computational details: All DFT calculations were carried out using Vienna *ab initio* simulation package (VASP) code. The projector augmented plane wave (PAW) method was employed for treating the electron–ion interactions; the electron exchange-correlation effects were accounted for within the framework of the generalized gradient approximation (GGA) using the PBE exchange-functional. The plane wave cutoff of 450 eV was used with using a standard Monkhorst–Pack grid (5×5×5 sampling mesh for bulk calculations and 4×4×1 for slab calculations). The full optimization of the system achieved with the convergence criterion was set to 10^{-4} eV. Bulk monoclinic CuO unit cell was obtained by optimizing the (1×1×1) cell. Perfect (020) surface of CuO slab was modeled using three layer symmetric slabs with vacuum widths of 15 Å. (020) surface with a necking edge including four layers is constructed by delimiting several oxygen and copper atoms in the middle of slab with vacuum width of 15 Å.

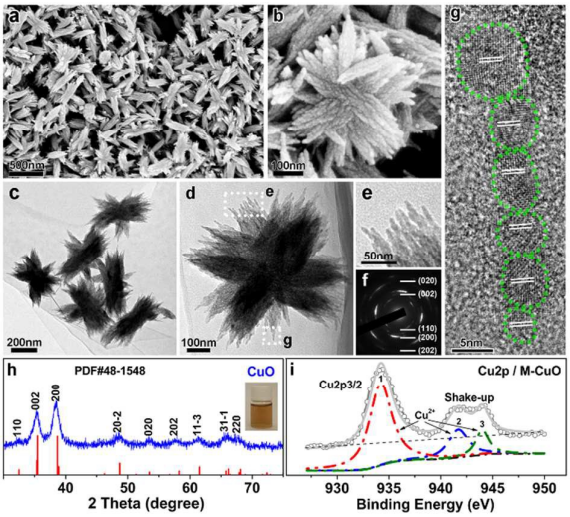

Fig. 1 Morphological and structural characterizations. (a) Low-magnification and (b) high-magnification SEM images of M-CuO. (c) Low-magnification and (d) high-magnification TEM images of M-CuO. (e) Enlarged image of selected area "e" in (d). (f) SAED pattern of a single M-CuO branch. (g) HRTEM image of selected area "g" in (d), the green dotted lines mark the contour of CuO nanoparticles and white double lines indicate CuO (020) planes with a spacing of ~1.7 nm. (h) XRD pattern of M-CuO; the inset is a photograph of aqueous solution of M-CuO. (i) XPS core-level spectrum of Cu2p in M-CuO, peaks located in 934.6, 941.6 and 943.7 eV originate from Cu^{2+} state.

Results and discussion

M-CuO was prepared via PLAL and subsequent oxidation (see experimental section in supporting information for details). The as-synthesized M-CuO consists of a lot of interconnected spindles (Fig. 1a). Each spindle is compose of many tiny branches with rough surface (Fig. 1b-1d). High-magnification SEM and TEM images illustrate that every branch contains many nanoparticles (Fig. 1b and 1e) which assemble along a preferential crystallographic orientation, as indicated by the high-resolution TEM (HRTEM) image (Fig. 1g). The selected area electron diffraction (SAED) pattern from a single branch (Fig. 1f) presents a set of single-crystal diffraction spots accompanied by elongated diffraction arcs, suggesting slight lattice misorientation between nanoparticulates. XRD pattern accords well with monoclinic CuO (PDF, No. 48-1548) (Fig. 1h), and XPS profile reveals Cu 2p3/2 peak of Cu^{2+} state as well as its shake-up satellites (Fig. 1i) [36,37]. By closely observing different branches of M-CuO, we found that the lattice is continuous (Fig. S1). Moreover, the interplanar spacings of nanoparticulates are 0.28, 0.23 and 0.17 nm, corresponding to (110), (200) and (020) planes, respectively, of monoclinic CuO.

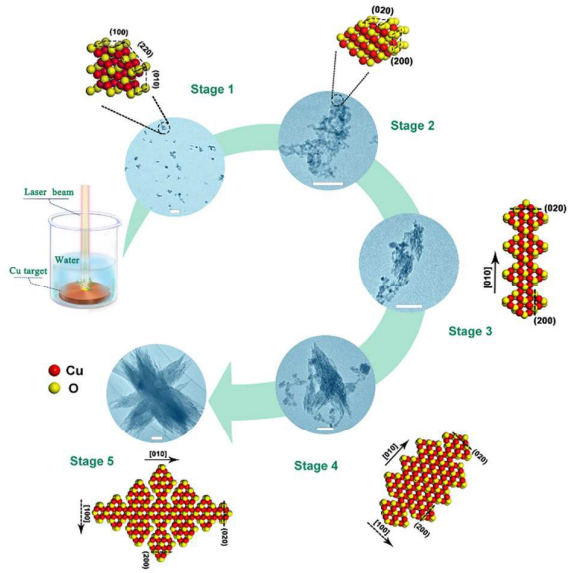

Fig. 2 Structural evolution from Cu_2O nanoparticles to M-CuO. Across the green arrow are the TEM images of each stage and corresponding crystal lattice models: Stage 1, initial Cu_2O nanoparticles obtained by PLAL. Stage 2, loosely agglomerate of CuO nanoparticles. Stage 3, an original cylindric M-CuO growing from agglomerate of CuO nanoparticles along [010] direction. Stage 4, oriented growth along [010] and [100] directions to form a spindle-like structure. Stage 5, hierarchically structured M-CuO obtained by further oriented growth. The scale bar is 50 nm.

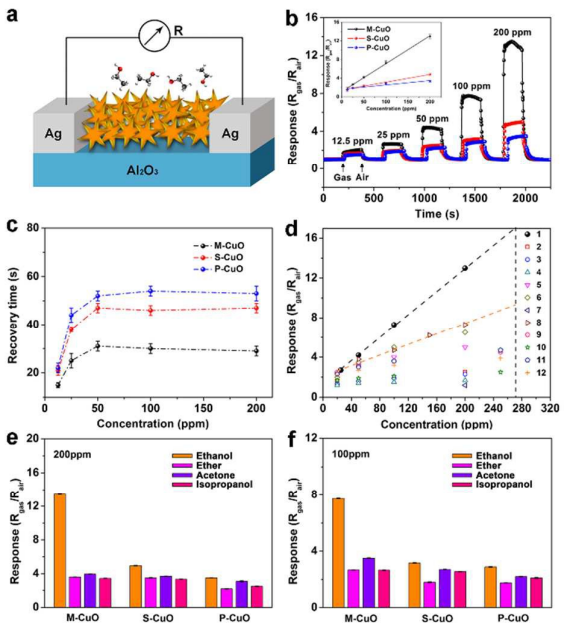

Fig. 3 Gas sensing properties of the devices constructed by using M-CuO, S-CuO and P-CuO at working temperature of 200 °C. (a) Schematic illustration of a gas-sensing device. (b) Real-time gas-sensing response of M-CuO, S-CuO and P-CuO toward ethanol under 12.5-200 ppm concentrations. The inserted plot is the linear fitting of sensitivities as a function of ethanol concentration for the three samples. (c) Gas-sensing recovery time as a function of ethanol concentration. (d) Comparison on the properties of M-CuO sensors with various CuO sensors reported in literatures: 1) M-CuO in this work, 2) CuO nanosheets[32], 3) CuO microspheres[31], 4) commercial CuO powder[31], 5) Ag-CuO heterojunction[31], 6) CuO nanorods[45], 7) CuO nanofilms[46], 8) CuO/In_2O_3 core-shell nanorods[47], 9) belt-like CuO[47], 10) willow-leaf-like CuO nanoplates[48], 11) quasi-square CuO nanoplates[48], 12) rod-like CuO[49]. (e) and (f) the sensing selectivity of M-CuO in 200 and 100 ppm gas concentration, respectively.

The HRTEM image exhibits an preferiential growth along [010] direction, which is confirmed by fast Fourier transform (FFT) pattern (insets in Fig. S1b-1h). All above results accords well with the previous reports on the mesocrystals assembled with tiny nanoparticles[1-3], demonstrating the successful synthesis of M-CuO.

In order to understand the growth process of M-CuO, we tracked the structural evolution during the synthetic process (see Fig. 2 and Fig. S2). At first, PLAL procedure yields dispersed nanoparticles with an average size of ~10 nm (Fig. S3) which are characterized as pure cubic cuprous oxide (Cu_2O) (PDF No. 05-0667) according to XRD and EDS analyses (Fig. S4a and S4b). The formation of oxide nanopaticles could be ascribed to the reaction of Cu nanoparticles generated by laser ablation with the dissolved oxygen in water. However, the content of the dissolved oxygen in water is limited, thus the oxidization cannot proceed thoroughly, giving rise to Cu_2O (instead of CuO) nanoparticles. Afterwards, they are gradually oxidized into CuO nanoparticles (Fig. S2b, Fig. S4c and S4d). Next, the CuO nanoparticles self-assemble into a loosely interconnected agglomerates (Stage 2), and further merge into original CuO cylinders along [010] orientation (Stage 3). Subsequently, CuO cylinders continue to grow along [010] and [100] directions by capturing CuO nanoparticles to form a spindle-like structure (Stage 4), which keeps growing and ripenning to develop into CuO bundles eventually (Stage 5). The detailed morphological evolution is given in Fig. S2.

To elucidate the formation mechanism of M-CuO, we first measured the change of zeta potential during the structural evolution. The zeta potential of Cu_2O precursors was determined as +49 mV immediatly after the PLAL synthesis (0 h, Fig. S5), hence, Cu_2O NPs can not aggregate due to the existence of the electrostatic repulsion[38-40]. As the oxidation proceeds, the zeta potential of Cu_2O NPs decreases gradually (Fig. S5), facilitating the aggregation of nanoparticles. We realize that (020) and (200) planes of CuO comprise oxygen atoms solely, thus being less positive than (110), (002) and (202) planes containning copper atoms (Fig. S6), resultantly, the CuO NPs come into contact with each other orderly along (020), (200) planes controlled by electrostatic force. Moreover, (020) plane owns higher surface energy than (200) plane, thus the growth along [010] direction is faster than that along [100] direction, giving rise to a spindle-like structure by the fusion of high-energy crystal faces[6, 41].

To verify above mechanism more rigorously, we added NaCl into Cu_2O precursor to weaken the the electrostatic repulsion by reducing the zeta potential to -0.6 ~ 0.5 mV. Resultantly, Cu_2O NPs aggregate quickly into disordered floccule whose morphology was kept after the oxidation. TEM observation

reveals that the final product is the agglomerate of disordered CuO nanoparticles, which is completely different from M-CuO (Fig. S7).

Next, we test the gas sensing performance of M-CuO. Three gas sensors were constructed by depositing M-CuO, S-CuO and P-CuO materials, respectively, on a cleaned alumina substrate with silver electrodes (Fig. 3a). Particularly, S-CuO and P-CuO were designed to possess similar morphology and exposed facets with M-CuO so as to make a easy comparison (Fig. S8 and S9)[42,43]. The optimum working temperature was determined as 200 ^{o}C according to the response-temperature relationship shown in Fig. S10.

Fig. 3b illustrates the real-time response of M-CuO, S-CuO and P-CuO with ethanol concentration varying from 12.5 to 200 ppm. The resistances increase abruptly for all devices upon ethanol exposure; when ethanol gas is exhausted, the resistances decrease to their initial values, indicating a good reversibility. Noticeably, the sensor response depends linearly on ethanol concentration over a wide range (inset of Fig. 3b). In particular, the response magnitude of M-CuO is much larger than those of S-CuO and P-CuO. Fig. 3c shows the recovery time (defined as the time required from 90% of the final equilibrium value to its initial value[44]) as the function of gas concentration. When the ethanol concentrations are lower than 50 ppm, the recovery time exhibits a positive correlation with gas concentration for all of CuO sensors, and it keeps constant once gas concentration is higher than 50 ppm. Whatsoever, the recovery time of M-CuO is significantly shorter than those of S-CuO and P-CuO.

As compared with various CuO structures reported in literatures (Fig. 3d, Table S1), M-CuO shows the best sensitivity (at least twice as much as other CuO structures) to ethanol. Meanwhile, M-CuO responds in a similar manner to other reducing gases (ether, acetone and isopropanol) with a better sensitivity than S-CuO and P-CuO (Fig. S11). Moreover, M-CuO senosr manifests itself a superior selectivity compared to S-CuO and P-CuO ones (Fig. 3e, 3f and Fig. S12). All of the above properties indicate that M-CuO is a charming material for gas sensing application.

The well-known sensing mechanism is based on the depletion theory of semiconductor materials[48]. Oxygen molecules in air adsorb onto the semiconductor surface and capture electrons, forming oxygen species (O_2^-, O_2^{2-}, O^-) and electron depletion layer. When exposed to a reductive gas, the depletion layer can be compensated by the electrons from adsorbed gas molecules, leading to the recovery of electron resistance[31,50]. Therefore, sensing response is intrinsically related to the surface state of semiconductor, including specific surface area[51], surface chemical composition[52], and valence states of elements[53,54], which can affect the oxygen adsorption significantly. Nitrogen adsorption-desorption measurement reveals that the specific surface area of M-CuO (52.5 m^2g^{-1}) is larger than those of S-CuO (39.2 m^2g^{-1}) and P-CuO (31.5 m^2g^{-1}) (Fig. S13). In addition, although the three samples owns identical composition and valence state of Cu^{2+} according to XPS and EDS profiles (Fig. S14), the peak area ratio of Cu^{2+} to lattice oxygen (O_L) (1.47) of M-CuO is higher than those of S-CuO (1.39) and P-CuO (1.35) (Fig. S15). Such a result indicates that M-CuO contains much more oxygen vacancies that serve as active sites for adsorbing oxygen molecules in air[55]. The high density of oxygen vacancies and large specific surface area endow M-CuO with more active sites and thicker depletion layer compared with S-CuO and P-CuO, which certainly favors the gas response.

However, even assuming that S-CuO and P-CuO are endued with the same surface area and oxygen vacancies with M-CuO, and the two parameters has a linear relationship with the final gas response, the calculated values of S-CuO and P-CuO are still much lower than the experimental values of M-CuO (Fig. S16). In fact, the effect of specific surface area and oxygen vacancies is not as obvious as the supposed linear correlation[31,50,53,54,56]. On the other hand, the CuO agglomerate obtained by adding NaCl possesses larger specific surface area than M-CuO, however, the gas sensitivity of CuO agglomerate is remarkably lower than M-CuO (Fig. S17). On the basis of the above, the superior properties of M-CuO cannot be explained simply from the point of view of specific surface area and oxygen vacancies.

Response sensitivity (R_{gas}/R_{air}) is determined by the resistance change of sensor in air and target gas, thus better response sensitivity requires lower initial resistance (R_{air}) and higher working resistance (R_{gas}). We measured the initial and working resistances of the three sensors. As shown in Fig. 4, the initial resistances are determined as ~560, ~2100 and ~8600 Ω for S-CuO, M-CuO and P-CuO, respectively, while the working resistance are of ~1800, ~16500 and 24000 Ω for S-CuO, M-CuO and P-CuO, respectively. Obviously, the high gas sensitivity of M-CuO originates from its moderate initial resistance and huge resistance change before and after the injection of ethanol.

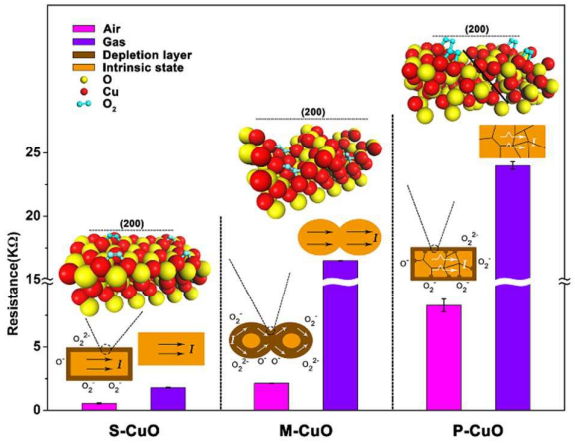

Fig. 4 Schematic sensing models for M-CuO, S-CuO and P-CuO. The bars represent the electrical resistances of each sample in air and in 100 ppm ethanol. Schematic diagrams on the top of the bars are electrical conduction states of S-CuO, M-CuO and P-CuO in air and in ethanol gas, respectively. The topmost images are the optimized configurations of oxygen molecules adsorbed on the CuO structures.

The initial resistance depends on the intrinsic crystalline structure as well as the thickness of surface depletion-layer caused by the absorption of oxygen molecules. Noticing that the three structures are composed of CuO with same phase structure (Fig. S8 and S9), the resistance difference should arise from the surface structure and grain boundary (Fig. S8, S9, S18). We then established the structural models according to experimental results (top image, Fig. 4) and performed density functional theory (DFT) calculation on the oxygen adsorption. The results indicate that the sites on necking edge (adsorption energy ΔE_{ads}= -3.63 eV) is more active for adsorbing oxygen molecules than that on smooth surface (ΔE_{ads}= -1.77 eV), more importantantly, the density of active sites in M-CuO is ten times of that in S-CuO (Fig. S19 and related calculation). Therefore, oxygen molecules can adsorb on necking sites of M-CuO more easily to produce thicker depletion layer than that in S-CuO and P-CuO.

The sensing mechanism of the three CuO structures can be understood as following. For S-CuO, there exists merely a thin depletion layer in air due to the rare adsorption sites, and electric current flows smoothly through the perfect internal structure[44], thus it exhibits the lowest R_{air} (~560 Ω). When S-CuO was exposed to ethanol gas, the recovery of thin depletion layer results in a limited resistance change and then low response sensitivity.

For P-CuO, a lot of grain boundaries cause a high initial resistance (~8600 Ω), meanwhile, the grain boundaries are apt to adsorb oxygen to generate a thicker depletion layer in air[44,57,58]. After being exposed to ethanol, the electric resistance increases significantly due to the elimination of thicker depletion layer. However, the high initial resistance counteracts the large resistance change, resulting in a similar performance with S-CuO.

In comparison with P-CuO and S-CuO, M-CuO displays a lower initial resistance (~2100 Ω) due to its quasi-monocrystal structure, meanwhile, it possesses abundant necking sites that give rise to thick depletion layer. Quantitatively, the thickness of depletion layer can be expressed by Debye length (L_D)[52].

$$L_D = \left(\frac{\varepsilon kT}{q^2 n_c}\right)^{\frac{1}{2}} \qquad (\varepsilon = \varepsilon_0 \times \varepsilon_s) \qquad (1)$$

where ε is the static dielectric constant, ε_0 the vacuum permittivity (8.85×10^{-12} F/m), ε_s the relative permittivity (25 for CuO), k the Boltzmann constant (1.38×10^{-23} J/K), T the absolute temperature (473 K), q the electrical charge of the carrier (1.6×10^{-19} C) and n_c the carrier concentration (1.96× 10^{18} cm^{-3})[59]. L_D is determined approximately as 5.4 nm for CuO which is larger than the average radius of component nanoparticles in M-CuO (4.5 nm, see Fig. S18b), therefore, the branches of M-CuO can be depleted completely. The quasi-continuous lattice and the complete depletion layer jointly contribute to the low initial resistance in air. While being exposed to ethanol, the fully depleted M-CuO can be recovered completely, causing a remarkable increase in electrical resistance and the highest sensitivity among the three CuO structures.

Conclusions

Template-free CuO mesocrytal was synthesized via a brand-new green synthetic process combining PLAL with slow oxidization in air. We found that the controlled oxidization can induce unevenly distributed surface charges and orientated attachment of CuO nanoparticles, giving rise to a spindle-like structure growing along [010] direction. We applied M-CuO architecture to gas sensor and achieved the ever-reported highest sensitivity, highest selectivity, and fastest recovery time to ethanol. We investigated the gas-sensing mechanism by comparing M-CuO with S-CuO and P-CuO, and found that the superior performance arises from the unique structure of M-CuO including quasi-monoscrystal lattice, numerous active sites and then fully depleted branches, which confers lower initial electrical resistance in air and higher working resistance in ethanol. Our work demonstrates that M-CuO is an excellent candidate for gas sensors, and further study will make effort on developing other mesocrystal materials for the detection of various gases.

Acknowledgements

This work was supported by the National Basic Research Program of China (2014CB931703), and the Natural Science Foundation of China (Nos. 51471115, 51502199, 21403152 and 51171127).

References

1 Y. Y. Kim, A. S. Schenk, J. Ihli, A. N. Kulak, N. B. Hetherington, C. C. Tang, W. W. Schmahl, E. Griesshaber, G. Hyett, F. C. Meldrum, *Nat. Commun.* 2014, **5,** 4341.
2 H. Cölfen, M. Antonietti, *Angew. Chem. Int. Ed.* 2005, **44,** 5576-5591.
3 R. Q. Song, H. Cölfen, *Adv. Mater.* 2010, **22,** 1301-1330.
4 A. W. Xu, M. Antonietti, H. Cölfen, Y. P. Fang, *Adv. Funct. Mater*. 2006, **16,** 903-908.
5 Y. Oaki, M. Kijima, H. Imai, *J. Am. Chem. Soc.* 2011, **133,** 8594-8599.
6 Z. P. Zhang, H. P. Sun, X. Q. Shao, D. F. Li, H. D. Yu, M. Y. Han, *Adv. Mater.* 2005, **17,** 43-47.
7 R. Q. Song, H. Cölfen, A. W. Xu, J. Hartmann, M. Antonietti, *ACS Nano*. 2009, **3,** 1966-1978.
8 X. Y. Wu, S. Yin, B. Liu, M. Kobayashi, M. Kakihana, T. Sato, *J. Mater. Chem. A.* 2014, **2,** 20832-20840.
9 P. Tartaj, J. M. Amarilla, *Adv. Mater.* 2011, **23,** 4904-4907.
10 R. C. Jin, J. H. Zhou, Y. S. Guan, H. Liu, G. Chen, *J. Mater. Chem. A.* 2014, **2,** 13241-13244.
11 J. Popovic, R. Demir-Cakan, J. Tornow, M. Morcrette, D. S. Su, R. Schlogl, M. Antonietti, M. M. Titirici, *Small*. 2011, **7,** 1127-1135.
12 E. Uchaker, M. Gu, N. Zhou, Y. W. Li, C. M. Wang, G. Z. Cao, *Small*. 2013, **9,** 3880-3886.
13 Z. S. Hong, M. D. Wei, T. B. Lan, L. L. Jiang, G. Z. Cao, *Energy Environ. Sci.* 2012, **5,** 5408-5413.
14 G. H. Yue, Y. Zhang, X. Q. Zhang, C. G. Wang, Y. C. Zhao, D. L. Peng, *Appl. Phys. A.* 2014, **118,** 763-767.
15 G. L. Li, Q. W. Chen, J. Lan, *ACS Appl. Mater. Interfaces.* 2014, **6,** 22561-22568.
16 H. G. Zhang, Q. S. Zhu, Y. Zhang, Y. Wang, L. Zhao, B. Yu, *Adv. Funct. Mater.* 2007, **17,** 2766-2771.

17 L. C. Jia, W. P. Cai, *Adv. Funct. Mater.* 2010, **20,** 3765-3773.
18 L. T. Duy, D. J. Kim, T. Q. Trung, V. Q. Dang, B. Y. Kim, H. K. Moon, N. E. Lee, *Adv. Funct. Mater.* 2015, **25,** 883-890.
19 R. S. Devan, R. A. Patil, J. H. Lin, Y. R. Ma, *Adv. Funct. Mater.* 2012, **22,** 3326-3370.
20 S. Z. Deng, V. Tjoa, H. M. Fan, H. R. Tan, D. C. Sayle, M. Olivo, S. Mhaisalkar, J. Wei, C. H. Sow, *J. Am. Chem. Soc.* 2012, **134,** 4905-4917.
21 J. M. Ma, J. Teo, L. Mei, Z. Y. Zhong, Q. H. Li, T. H. Wang, X. C. Duan, J. B. Lian, W. J. Zheng, *J. Mater. Chem.* 2012, **22,** 11694-11700.
22 X. Liu, J. B. Sun, X. T. Zhang, *Sensors and Actuators B.* 2015, **211,** 220-226.
23 C. Su, Y. C. Zou, X. F. Xu, L. Liu, Z. Liu, L. L. Liu, *Colloids and Surfaces A: Physicochem. Eng. Aspects.* 2015, **472,** 63–68.
24 J. G. Cai, S. Y. Chen, M. Ji, J. Hu, Y. R. Ma, L. M. Qi, *CrystEngComm*. 2014, **16,** 1553-1559.
25 Z. F. Bian, T. Tachikawa, P. Zhang, M. Fujitsuka, T. Majima, *Nat. Commun*. 2014, **5,** 3038.
26 J. Fang, B. Ding, X. Song, *Appl. Phys. Lett.* 2007, 91, 083108.
27 S. S. Wang, A. W. Xu, *CrystEngComm*. 2013, **15,** 376-381.
28 K. Y. Niu, J. Yang, S. A. Kulinich, J. Sun, H. Li, X. W. Du, *J. Am. Chem. Soc.* 2010, **132,** 9814-9819.
29 J. Yang, T. Ling, W. T. Wu, H. Liu, M. R. Gao, C. Ling, L. Li, X. W. Du, *Nat. Commun.* 2013, **4,** 1695.
30 R. C. Luo, C. Li, X. W. Du, J. Yang, *Angew. Chem. Int. Ed.* 2015, **54,** 4787-4791.
31 G. X. Zhu, H. Xu, Y. Y. Xiao, Y. J. Liu, A. H. Yuan, X. P. Shen, *ACS Appl. Mater. Interfaces*. 2012, **4,** 744-751.
32 H. Y. Yan, X. Q. Tian, J. Sun, F. G. Ma, *J Mater Sci: Mater Electron*. 2014, **26,** 280-287.
33 X. H. Liu, J. Zhang, Y. F. Kang, S. H. Wu, *CrystEngComm,* 2012, **14**, 620-625.
34 S. Harish, M. Navaneethan, J. Archana, S. Ponnusamy, C. Muthamizhchelvan, Y. Hayakawa, *Materials Letters*. 2015, **139,** 59-62.
35 X. J. Zhang, G. F. Wang, X. W. Liu, J. J. Wu, M. Li, J. Gu, H. Liu, B. Fang, *J. Phys. Chem. C.* 2008, **112,** 16845-16849.
36 C. C. Chusuei, M. A. Brookshier, D. W. Goodman, *Langmuir.* 1999, **15,** 2806-2808.
37 M. Yin, C. K. Wu, Y. B. Lou, C. Burda, J. T. Koberstein, Y. M. Zhu, S. O'Brien, *J. Am. Chem. Soc.* 2005, **127,** 9506-9511.
38 T. Kim, K. Lee, M. S. Gong, S. W. Joo, *Langmuir*. 2005, **21,** 9524-9528.
39 R. P. Bagwe, L. R. Hilliard, W. H. Tan, *Langmuir*. 2006, **22,** 4357-4362.
40 J. K. Jiang, G. Oberdörster, P. Biswas, *J. Nanopart. Res.* 2009, **11,** 77-89.
41 B. Liu, H. C. Zeng, *J. Am. Chem. Soc.* 2004, **126,** 8124-8125.
42 Z. Y. Jiang, Q. Kuang, Z. X. Xie, L. S. Zheng, *Adv. Funct. Mater.* 2010, **20,** 3634-3645.
43 X. X. Xu, J. Zhuang, X. Wang, *J. Am. Chem. Soc.* 2008, **130,** 12527-12535.
44 A. Gurlo, R. Riedel, *Angew. Chem. Int. Ed.* 2007, **46,** 3826-3848.
45 C. Yang, X. T. Su, F. Xiao, J. K. Jian, J. D. Wang, *Sensors and Actuators B.* 2011, **158,** 299-303.
46 A. S. Zoolfakar, M. Z. Ahmad, R. A. Rani, J. Z. Ou, S. Balendhran, S. Zhuiykov, K. Latham, W. Wlodarski, K. Kalantar-zadeh, *Sensors and Actuators B.* 2013, **185,** 620-627.
47 S. H. Park, H. S. Ko, S. Y. An, W. I. Lee, S. M. Lee, C. M. Lee, *Ceramics International*. 2013, **39,** 5255-5262.
48 C. Yang, F. Xiao, J. D. Wang, X. T. Su, *J. Colloid Interface Sci.* 2014, **435,** 34-42.
49 N. Nasiri, R. H. Bo, F. Wang, L. Fu, A. Tricoli, *Adv. Mater.* 2015, **27,** 4336-4343.
50 D. P. Volanti, A. A. Felix, M. O. Orlandi, G. Whitfield, D. J. Yang, E. Longo, H. L. Tuller, J. A. Varela, *Adv. Funct. Mater.* 2013, **23,** 1759-1766.
51 Y. Y. Lü, W. W. Zhan, Y. He, Y. Y. Wang, X. J. Kong, Q. Kuang, Z. X. Xie, L. S. Zheng, *ACS Appl. Mater. Interfaces*. 2014, **6,** 4186-4195.
52 L. I. Trakhtenberg, G. N. Gerasimov, V. F. Gromov, T. V. Belysheva, O. J. Ilegbusi, *Sensors and Actuators B.* 2015, **209,** 562-569.
53 D. J. Yang, I. Kamienchick, D. Y. Youn, A. Rothschild, I. D. Kim, *Adv. Funct. Mater.* 2010, **20,** 4258-4264.
54 J. J. Wu, Q. W. Huang, D. W. Zeng, S. P. Zhang, L. Yang, D. S. Xia, Z. D. Xiong, C. S. Xie, *Sensors and Actuators B.* 2014, **198,** 62-69.
55 F. Tian, L. Zhao, X. Y. Xue, Y. Shen, X. Jia, S. Chen, Z. Wang, *Applied Surface Science.* 2014, **311,** 362-368.
56 J. W. Zhao, C. S. Xie, L. Yang, S. P. Zhang, G. Z. Zhang, Z. M. Cai, *Applied Surface Science.* 2015, **330,** 126-133.
57 M. W. Ahn, K. S. Park, J. H. Heo, J. G. Park, D. W. Kim, K. J. Choi, J. H. Lee, S. H. Hong, *Appl. Phys. Lett.* 2008, **93,** 263103.
58 L. M. Li, Z. F. Du, T. H. Wang, *Sensors and Actuators B.* 2010, **147,** 165-169.
59 D. Gopalakrishna, K. Vijayalakshmi, C. Ravidhas, *Ceramics International*. 2013, **39,** 7685-7691.